Vapor assisted deposition of highly efficient, luminescent and stable black phase $FAPbI_3$ perovskite solar cells

Haizhou Lu[1,2,3], Yuhang Liu[2], Paramvir Ahlawat[4], Aditya Mishra[5], Wolfgang R. Tress[1], Felix T. Eickemeyer[2], Zaiwei Wang[1], Claudia E. Avalos[5], Brian I. Carlsen[1], Anand Agarwalla[1], Xin Zhang[3], Xiaoguo Li[3], Yiqiang Zhan[3*], Shaik M. Zakeeruddin[1,2], Lyndon Emsley[5], Ursula Rothlisberger[4], Lirong Zheng[3*], Michael Grätzel[2*], Anders Hagfeldt[1*]

[1]Laboratory of Photomolecular Science, Institute of Chemical Sciences Engineering, École Polytechnique Fédérale de Lausanne (EPFL), CH-1015 Lausanne, Switzerland.
[2]Laboratory of Photonics and Interfaces, Institute of Chemical Sciences and Engineering, École Polytechnique Fédérale de Lausanne (EPFL), CH-1015 Lausanne, Switzerland.
[3]Centre for Micro Nano Systems, School of Information Science and Technology (SIST), Fudan University, Shanghai 200433, P. R. China.
[4]Laboratory of Computational Chemistry and Biochemistry, Institute of Chemical Sciences and Engineering, École Polytechnique Fédérale de Lausanne (EPFL), CH-1015 Lausanne, Switzerland.
[5]Laboratory of Magnetic Resonance, Institute of Chemical Sciences and Engineering, École Polytechnique Fédérale de Lausanne (EPFL), CH-1015 Lausanne, Switzerland.

Abstract

Mixtures of cations or halides with $FAPbI_3$ are being used practically in all high efficiency perovskite solar cells (PSCs). However, this comes at the cost of blue shifted light absorption. Moreover, mixed cations or halides cause long-term stability issues due to the loss of volatile methylammonium and phase segregation. Obtaining efficient and stable $FAPbI_3$ based PSCs is of vital importance for the perovskite research field. Here, we report a novel deposition method employing MASCN vapor treatment to convert yellow δ-$FAPbI_3$ perovskite films to the desired pure α-phase. Molecular dynamics simulations show that the SCN^- anions play a key role in promoting the formation and stabilization of α-$FAPbI_3$ below the thermodynamic phase transition temperature. This agrees with the fact that the phase transition can also be triggered by using FASCN instead of MASCN for the vapor treatment. We exploit this discovery to produce $FAPbI_3$ films which show a very low defect density level allowing the realization of PSCs with > 23% power conversion efficiency showing long term operational and thermal stability as well as a record low (330 mV) Voc loss over band gap and a record low (0.75 V) turn-on voltage of electroluminescence.

Metal halide perovskites are being widely investigated in many fields, including solar cells [1-10], light-emitting diodes (LEDs) [11-15], lasers [16] and photodetectors [17, 18]. Within a decade, power conversion efficiencies (PCEs) of perovskite solar cells (PSCs) have been increasing from around 3.8% [19] to 25.2% [20] exceeding other thin film solar cells and the market leader polycrystalline silicon. Since 2015, formamidinium (FA) has been used as the preferred cation in almost all high efficiency PSCs, because FA based formulations are thermally more stable than perovskites containing methylammonium (MA) and its narrower bandgap is closer to the Shockley-Queisser optimum [4]. Our previous molecular dynamics studies show that FA reorientation is faster than that of MA on the A cation site of the perovskite, which leads to enhanced stabilization and slower charge carrier recombination [21, 22]. Also, $FAPbI_3$ has a Goldschmidt tolerance factor of 0.99 [2], which suggests a perfect crystalline perovskite structure with minimum distortions. Therefore, $FAPbI_3$ perovskite could be an ideal candidate for efficient, and stable PSCs.

Unfortunately, a photoinactive δ form of $FAPbI_3$ is the most stable phase at room temperature, and the crystallinity of $FAPbI_3$ film is normally poor even after high temperature annealing. To avoid formation of the δ-phase and improve the crystallinity, various complex perovskite compositions have been developed. For example, MA, Cs and/or Br are commonly mixed with $FAPbI_3$, especially for the record high efficiency PSCs [2-3, 5-6]. However, these mixed perovskite compositions show an unwanted blue shift in their light absorption. Moreover, the mixed perovskite precursor solutions can easily form precipitates when they are used for scale-up fabrications. Furthermore, MA is thermally unstable [4, 23], while Br/I mixtures suffer from severe ion segregations under light illuminations [24]. Thus, a mixing strategy may be unfavourable regarding long-term operational stability. Our previous work shows that mixing Cs and Rb with $FAPbI_3$ could be an alternative way to improve the operational stability [4], however, the resulting PCE is still behind that reported for most efficient PSCs. Hence obtaining efficient, phase pure and stable $FAPbI_3$ perovskite layers is of vital importance for the perovskite research field.

In contrast to the previous mixing strategies, manipulation of surface energy has been reported to stabilize the perovskite phases and modify the growth orientations [25-28]. For example, templated growth of oriented layered perovskites has been demonstrated for 2D perovskites [28], and epitaxial growth and stabilization of $FAPbI_3$ has been reported recently [29]. Swarnkar *et al*. showed that α-$CsPbI_3$ can be stabilized in the form of colloidal quantum dots due to a large contribution of surface energy [26]. Fu *et al*. reported that functionalizing the surface of $FAPbI_3$ with big organic molecules could lower the formation energy to stabilize the cubic $FAPbI_3$ phase at room temperature [27]. However, the performance and/or the stability of these systems are still poor comparing with those of mixed-cation-halide PSCs [25].

Motivated by these promising strategies of surface energy manipulations and our recent work using polyiodide vapor for scalable perovskites [30], we developed a novel methylammonium thiocyanate (MASCN) vapor treatment for preparing efficient and stable $FAPbI_3$ based PSCs. Figure 1(a) illustrates the steps of this vapor treatment process. Yellow colour δ-$FAPbI_3$ film was obtained by spin-coating a precursor solution of equal molar FAI and PbI_2 mixture. The as fabricated δ-$FAPbI_3$ film was immediately annealed at 100 ℃ for one minute. Then, the annealed film was put in a MASCN vapor environment for 5 seconds until the yellow colour changed to black. It should be noted that this vapor treatment was done under normal pressure as MASCN has a sublimation point below 100 ℃, which renders the whole treatment process low-cost and of practical interest for industrial scale-up applications.

Figure1(b) shows XRD data of $FAPbI_3$ perovskite films before and after exposure to MASCN vapor, confirming a structural transformation from yellow δ-phase to pure black α-phase. XRD data of $FAPbI_3$ films fabricated with conventional method (reference $FAPbI_3$) is also shown for comparison. Our results demonstrate that the reference $FAPbI_3$ films contain the yellow δ phase. However, for the vapor treated $FAPbI_3$ films, the δ-phase is effectively suppressed, and the full-width-half-maxima of the reflection peaks are decreased accordingly due to the increased XRD intensities indicating an increase in film crystallinity. In particular, the preferred orientation along the (001) plane reflects a change of surface energy during the crystallisation processes [31]. Figure 1(c) illustrates the UV-vis absorption and the photoluminescence (PL) spectra of the reference and vapor treated $FAPbI_3$ films. It shows identical absorption onsets as well as PL peaks at 812 nm, which implies that the vapor treatment does not induce a bandgap change. However, vapor treated $FAPbI_3$ films show stronger absorption over all wavelengths compared to the untreated reference sample, which is in accordance with the enhanced phase purity and crystallinity apparent from the XRD results.

We note that our work is different from some recent studies using MACl as an additive [5, 32-33], where a considerable amount of MA was doped inside the bulk $FAPbI_3$. Comparing with the previously reported results [5, 32], our UV-vis absorption/PL emission is red shifted. From the scanning electron microscopy (SEM) top-view images, shown in Figures 1(d) and 1(e), the grain size of $FAPbI_3$ films increases after vapor treatment. AFM images of the reference and vapor treated $FAPbI_3$ films show that the surface roughness is around 15 nm (shown in Figure S1). Figures 1(f) and 1(g) illustrate cross-sectional SEM images, showing that the irregular reference $FAPbI_3$ perovskite crystals convert to monolithic grains from the top to the bottom after the vapor treatment. In summary, our XRD data as well as SEM images show that the vapor treatment with MASCN induces a yellow δ to black α-phase transformation below the phase transition temperature together with a recrystallization of the α-phase $FAPbI_3$ films.

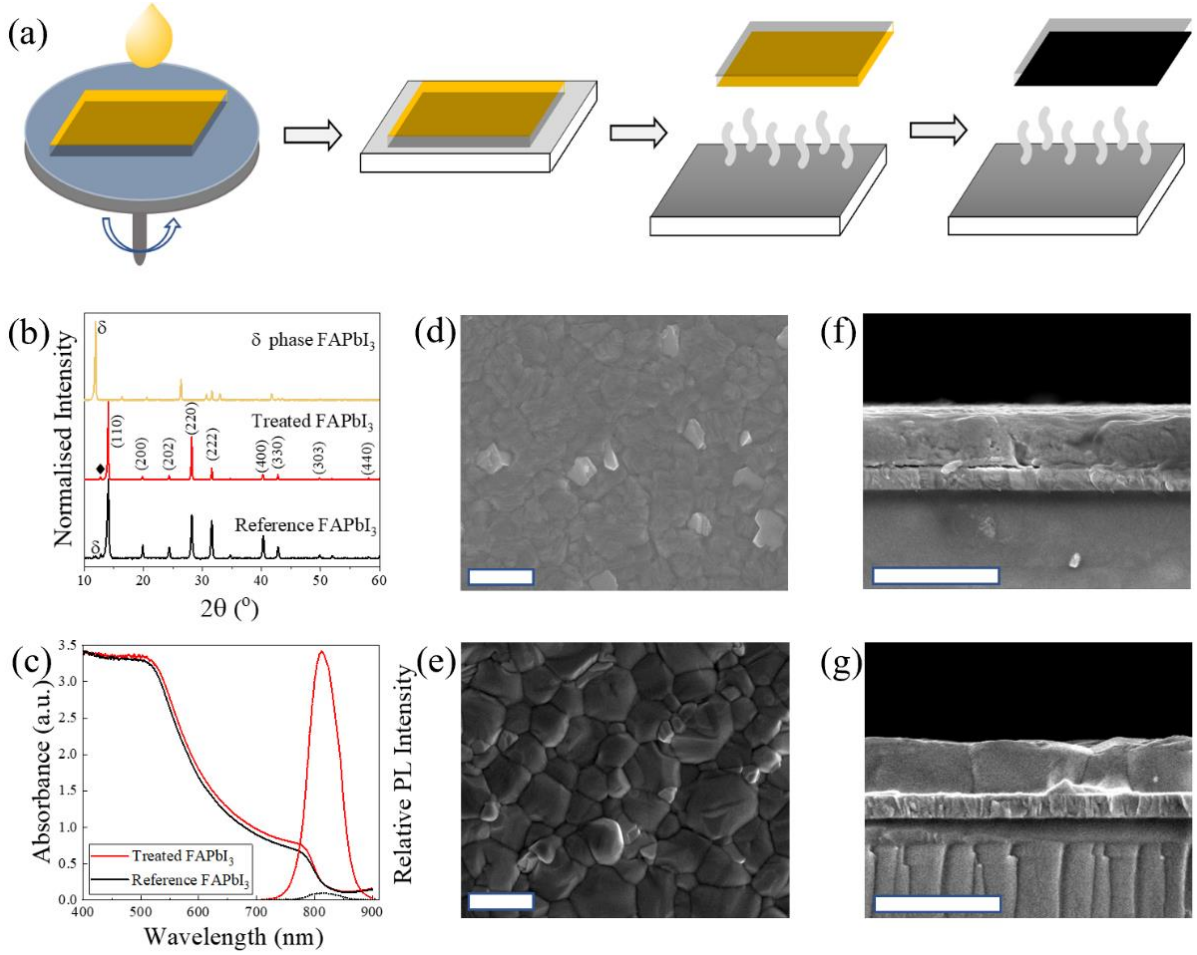

Figure 1*. Simplified scheme presenting the MASCN vapor treatment process for pure black phase $FAPbI_3$ perovskite films **(a)**; XRD patterns of $FAPbI_3$ perovskite films before (yellow colour) and after (red colour) vapor treatments, as well as the reference $FAPbI_3$ perovskite films fabricated with conventional method, ♦ indicates PbI_2 species **(b)**; UV-vis absorption and PL spectra of vapor treated and reference $FAPbI_3$ perovskite films **(c)**; top-view SEM images of the reference $FAPbI_3$ perovskite films **(d)** and vapor treated $FAPbI_3$ perovskite films **(e)**; cross-sectional SEM images of the reference $FAPbI_3$ perovskite films **(f)** and vapor treated $FAPbI_3$ perovskite films **(g)**. Scale bar is 1 µm.*

In order to unravel the role of MASCN during the vapor treatments, we carried out solid-state nuclear magnetic resonance (ssNMR) spectroscopy measurements. Recently, we and others

have shown that ssNMR is a powerful tool to identify cation incorporation [22, 34-36], halide-mixing [37], cation dynamics [21] and atomic-level interface interactions [38] in PSCs. We first carried out ^{14}N magic angle spinning (MAS) NMR measurements to investigate the effect of atomic-level interaction from the MASCN presence on the intrinsic crystallographic symmetry of the parent $FAPbI_3$ lattice. The ^{14}N MAS NMR spectra of $FAPbI_3$ features a ^{14}N spinning sideband (SSB) pattern, which corresponds to FA cation reorientation on the picosecond timescale [21]. Figures 2(a) and 2(b) indicate that the SSB width is altered by the MASCN surface treatment. It has been shown previously that the width of the ^{14}N SSB manifold is correlated with the symmetry of the cuboctahedra cavity in which FA cation reorientation takes place, whereby a narrower manifold indicates a symmetry closer to cubic [21-22, 35]. MASCN treated $FAPbI_3$ thin film features 3-4 orders of SSB less in ^{14}N spectrum compared to the reference $FAPbI_3$, indicative that FA is in a more symmetric environment. Note that, for both the reference and the treated $FAPbI_3$, the central peak of the ^{14}N MAS NMR spectra has identical shift. We conclude that MASCN is most likely interacting with the surface of the $FAPbI_3$ perovskites [39].

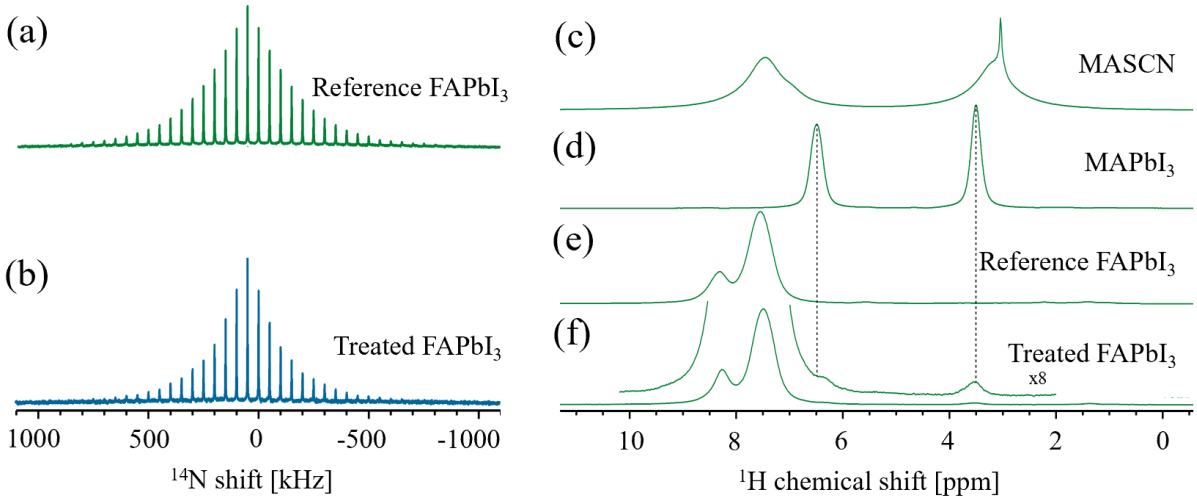

***Figure 2**. ^{14}N solid state MAS NMR spectra at 21.1 T, 298 K and 5 kHz MAS of the reference $FAPbI_3$ perovskites **(a)**, and vapor treated $FAPbI_3$ perovskites **(b)**; ^{1}H MAS NMR spectra at 21.1 T, 298 K and 20 kHz MAS of MASCN powder **(c)**, bulk-mechanochemical $MAPbI_3$ **(d)**, reference $FAPbI_3$ perovskites **(e)**, and vapor treated $FAPbI_3$ perovskites **(f)**.*

We carried out ^{1}H MAS ssNMR experiments to assess the amount of MA cation that is present in $FAPbI_3$ after the MASCN treatment. Figure 2(c) shows ^{1}H spectrum of MASCN powder which identifies two distinct ^{1}H environments corresponding to CH_3 at 3.05 and NH_3^+ at 7.45 ppm. $MAPbI_3$ and reference $FAPbI_3$ perovskites yielded signals at 3.5, 6.5 ppm corresponding to MA (Figure 2(d)) and at 7.5, 8.2 ppm corresponding to FA (Figure 2(e)). Figure 2(f) shows the ^{1}H spectrum of treated $FAPbI_3$ perovskites, which is identical to that of the reference $FAPbI_3$. When the signal is enhanced 8 times, small additional peaks at 3.5 and 6.3 ppm confirm that MA is present at very small levels in a $MA_xFA_{1-x}PbI_3$ environment, and not present as MASCN or any other form of MA. In order to quantify the amount of MA in the treated $FAPbI_3$ film, we carried out quantitative solid-state one-dimensional measurements where the integral over the peak suggests the amount of the respective species. Herein, the integral over the MA peak suggests up to 1.8% of MA in this vapor treated $FAPbI_3$ films (Supplementary note 1). We conclude that during the first stage of the MASCN vapor treatment, MA is incorporated into the surface of hexagonal $FAPbI_3$ films, which initialized the phase

transformation process. The relatively weak MA signal suggests that the majority of MASCN re-evaporated during the annealing procedure, which is consistent with the identical XRD peaks and optical absorbance spectra of the reference and treated $FAPbI_3$ films.

We further performed molecular dynamics (MD) simulations to gain atomic level insights of the vapor treatment process. The computational setup of the system that mimics the experimental procedure is shown in Figure S2. Simulation details as well as movies of the MD trajectories are given in SI. First, we present the analysis of the effects of SCN^- ions on the surface of hexagonal $FAPbI_3$. We find that SCN^- ions do not diffuse inside the face-sharing structure of δ-$FAPbI_3$ but remain at the surface (shown in supporting movie 1). Due to their strong affinity to Pb^{2+} ions, SCN^- anions coordinate to Pb^{2+} on the surface of hexagonal $FAPbI_3$ (shown in supporting movies 2 and 3). In particular, we find that Pb^{2+} ions are coordinated with the sulfur atoms of SCN^-, shown in Figure S3. Due to this strong interaction, SCN^- ions replace the iodides around the Pb^{2+} ions, which disintegrates the top layer of face-sharing octahedra and induces the transition to the corner-sharing architecture of α-$FAPbI_3$. Furthermore, the disruption of the topmost surface layer with SCN^- ions also helps the penetration of monovalent cations (MA^+) into the PbI_6 chains of hexagonal $FAPbI_3$, which further helps the growth of α-$FAPbI_3$. This is shown in supporting movie 4, and is also in agreement with our ssNMR analysis above. We further investigated the re-arrangement of ions at the surface of hexagonal $FAPbI_3$. We find that some parts of face-sharing octahedra on the interface starts to form corner-sharing Pb-I-SCN structures. With the addition of extra SCN^- ions, corner-sharing structures, which contain mixtures of SCN^- ions and iodides, are formed and stabilized. The atomic view of this whole transformation from face-sharing to corner-sharing octahedra is shown in Figure 3 and supplementary movies 5 and 6. Further analysis reveals that the conversion of the face-sharing structure proceeds via formation of edge-sharing intermediates. This results mainly from the step by step addition of SCN^- ions around the Pb^{2+} ions as seen in supplementary movies 5 and 6. Our previous studies have also shown formation of such intermediate structures before conversion to perovskites [40]. We further observe some particular domains of the mixed corner and face-sharing structures during the simulation and find that SCN^- ions can also induce the formation of polytypes at the interface. We observe the formation of localized structures similar to the well-known 4H polytypes of $FAPbI_3$ (shown in supplementary movies 6 and 7 and Figure S4). We also generate a model of a periodic structure of 4H polytype with iodides replaced by SCN^- and find this structure remains stable after DFT optimization (shown in SI). From this insight we conclude that SCN^- ions drive and stabilize the formation of corner-sharing structures upon contact formation with MASCN, which in turn trigger the conversion to α-$FAPbI_3$. Strikingly, this process can occur below the thermodynamic phase transition temperature.

In order to confirm the important role of SCN^-, we used FASCN instead of MASCN for the vapor treatment of the hexagonal phase $FAPbI_3$. Figure S5 shows that this results in the formation of pure α-$FAPbI_3$ even at an annealing temperature of only 100 ℃, which is far below the thermodynamic phase transition temperature. By contrast, in the absence of FASCN, the reference $FAPbI_3$ films annealed at 100 ℃ show mainly the formation of δ-phase. Thus, the complete transformation from the δ-$FAPbI_3$ to α-$FAPbI_3$ also occurs in the absence of MA^+ ions, which agrees well with our MD simulations.

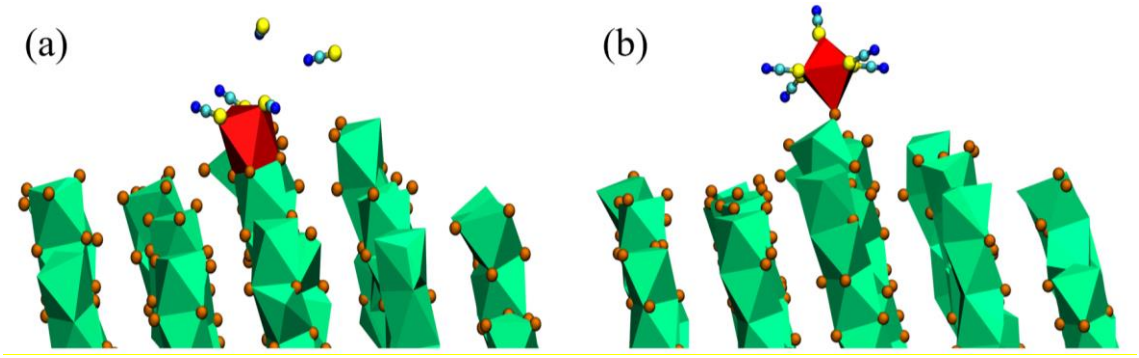

Figure 3. *Representative snapshot from the MD simulations showing conversion of the initial face-sharing octahedra* ***(a)*** *and corner-sharing octahedra* ***(b)****. Pb-I octahedra are shown with green color with iodide as orange balls on corners. To highlight the structural transformation, red color is chosen for octahedra on the interface.* FA^+ *and* MA^+ *ions are not shown for clarity. Selected* SCN^- *ions are shown with ball and sticks representation: sulfur with yellow, carbon with light blue and nitrogen with dark blue balls (the other* SCN^- *ions are not shown for the sake of clarity).*

Following the successful preparation of pure α-$FAPbI_3$ with ordered and monolithic grains, we further investigated the performance of the corresponding PSCs. All PSCs were fabricated using regular n-i-p structures (glass/ITO/SnO_2/perovskite/Spiro-MeOTAD/Au), shown in Figure 4(a). A cross-sectional SEM image of the full device structure is given in Figure S6. Figure 4(b) demonstrates a PCE of 23.1% for one of our champion $FAPbI_3$ PSCs with a J_{SC} of 24.4 mA/cm^2, V_{OC} of 1.165 V and fill factor (FF) of 81.3%. It also exhibits negligible hysteresis under both forward and reverse scans between 0 and 1.2 V. Details on the reproducibility of this vapor treatment technique are provided in Figure S7.

We checked the performance of our PSCs at the Photovoltaic Laboratory of the Institute of Micro Technique (IMT), Neuchâtel, Switzerland. The Wacom high-precision class AAA solar simulator available at the IMT PV-lab very closely mimics the solar spectrum in the absorption range of the PSCs in the range of 350 to 850 nm, avoiding any substantial spectral mismatch between the simulated and true AM 1.5G solar light source. The solar spectrum of Wacom lamp is given by the insert in Figure S8(a). An efficiency of 22.4% was confirmed under MPP condition in IMT, which is close to the measured 22.8% in our lab (shown in Figure S8). As a comparison, the J-V curves of the reference PSCs (without the vapor treatment) are given in Figure S9, which shows a relatively poor performance and large hysteresis. Figure 4(c) shows the corresponding IPCE curve and a projected J_{SC} of 24.3 mA/cm^2, obtained by integrating the IPCE over the AM 1.5G standard spectrum. This value matches well the J_{SC} of 24.4 mA/cm^2, measured under the solar simulator. Steady state power output at maximum power point (MPP) under one sun light soaking conditions is shown in Figure S10. The quick response and stable output indicate efficient charge extraction and negligible charge accumulation.

Once efficient carrier collection is achieved, the open circuit voltage becomes the main limiting factor for the device efficiency. Figure 4(d) illustrates a V_{OC} of 1.19 V obtained for one of the vapor treated $FAPbI_3$ based PSCs. The J-V curves for this device were measured under a cooling air flow at 20.1 ℃. The detailed determination of the measured V_{OC} is shown in Supplementary note 2. The temporal evolution of the V_{OC} measured for 5 mins under 0.9 Sun is shown in Figure S11. Over this time period the V_{OC} reaches a stable plateau. From the emission spectra (Figure 4(e)), we determine an Urbach energy of 14 meV (Figure S12). Using

this data, the IPCE and the reciprocity relation [41], we determine the theoretical radiative limit V_{OC} to be ~1.255 V (see SI for details of this calculation and the influence of temperature (Figure S13)). Thus, our measured V_{OC} is only 65 mV below the radiative limit and the voltage loss compared to the bandgap is only 330 mV. We derived a band gap of 1.52 eV for $FAPbI_3$ using the Tauc plot shown in Figure S14, which is somewhat larger than literature values [42]. To the best of our knowledge, our $FAPbI_3$ devices have the smallest V_{OC} loss reported so far for PSCs, outperforming silicon solar cells, and closely approaching that of GaAs photovoltaics [43]. It is well known that the V_{OC} value is related to density of defect of the perovskite layer acting as centres for non-radiative recombination of photo-generated charge carriers. To check on this loss channel, we measured the time-resolved photoluminescence (TRPL) of the reference and vapor treated $FAPbI_3$ films. Figure S15 shows that the lifetime of the treated $FAPbI_3$ is 299.3 ns, which is 3.7 times longer that of the reference film.

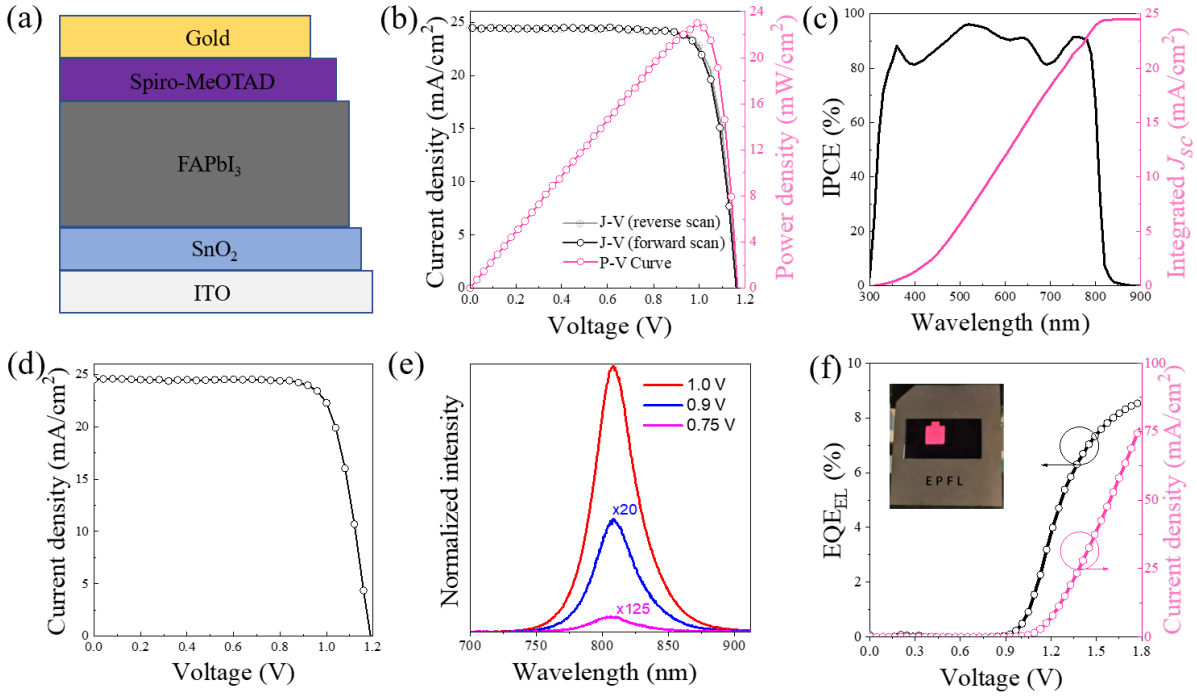

Figure 4*. A simplified graph of planar structure $FAPbI_3$ perovskite solar cells* ***(a)****; J-V curves under both reverse and forward scan directions, and power outputs under different bias voltages* ***(b)****; IPCE curve of $FAPbI_3$ perovskite solar cells over 300 nm to 900 nm wavelengths, and integrated J_{SC} over AM 1.5G standard spectrum* ***(c)****; J-V curve of $FAPbI_3$ perovskite solar cells with a V_{OC} of 1.19 V (measured at T=20.1 ℃)* ***(d)****; EL spectra of $FAPbI_3$ perovskite solar cells under different bias voltages from 0.75 V to 1 V* ***(e)****; EQE_{EL} and current density of $FAPbI_3$ perovskite solar cells under bias voltages from 0 to 1.8 V, a photograph of the luminescence of $FAPbI_3$ perovskite solar cell under 1.45 V bias voltage is inserted* ***(f)****.*

A solar cell's photovoltage is directly related to the ability to extract its internal luminescence, as derived by Ross [44]:

$$V_{oc} = V_{oc,rad} + \frac{kT}{q}\ln(\eta_{ext})$$

where V_{oc} is the expected open-circuit voltage, $V_{oc,rad}$ is the radiative limit of open-circuit voltage and η_{ext} is the external luminescence quantum efficiency. For any solar cell technology to approach the radiative limit, efficient external electroluminescence (EL) is a necessity [45].

Because we obtained a V_{OC} approaching the radiative limit $V_{oc,rad}$, we expected a high EQE_{EL} from our $FAPbI_3$ based PSCs. Figure 4(e) shows the EL spectra of $FAPbI_3$ based PSCs, which were measured under different bias voltages in ambient conditions. It shows a EL peak position at 810 nm, consistent with the above PL results. We detect EL emission already under a low bias voltage of 0.75 V. It is understood that thermal activation can contribute to reduce the turn-on voltage below the bandgap/q of the active/emissive semiconductor. To the best of our knowledge, 0.75 V is the lowest reported turn-on voltage value for perovskite-based devices, which suggests low leakage currents and/or energy loss, a perfect balanced carrier injection and low nonradiative recombination. Figure 4(f) shows an EQE_{EL} of 6.5% for an injection current density of 25 mA/cm^2 (corresponding to the short circuit current density measured under one sun illumination), which translates into a non-radiative loss as low as 70 mV (see Supplementary note 2), clearly surpassing the reported values in the literature and even light emission from the best silicon solar cells. We note that the measured EQE_{EL} is actually underestimated, as we have substantial emission losses via glass sheets, which could partially explain the 5 mV difference between the measured and predicted non-radiative loss. An even higher 8.6% EQE_{EL} is achieved with an injected current density below 100 mA/cm^2. These EQE_{EL} values are among the highest ones reported in the literature. Compared to the results published very recently [5, 45], our driving voltage is substantially smaller, resulting in an exceptional high peak wall-plug efficiency of 7.5% with a low bias voltage of 1.55 V, shown in Figure S16. Importantly, our devices exhibit a low roll-off under injected current densities up to 300 mA/cm^2, shown in Figure S17. This contrasts with the difficulties to reach high efficiency at high current densities, which has been a challenge for the other reported perovskite devices [5, 46], as well as organic LEDs [13]. Hence, our $FAPbI_3$ based PSCs compare favourably with the state-of-the-art perovskite-based LEDs, and even other organic LEDs.

We investigated the operational stability of our $FAPbI_3$ based PSCs as stability issues remain the main obstacle towards the commercialisations of PSCs. To the best of our knowledge, information on long-term stability under MPP tracking conditions (operational stability) is still scarce for PSCs with a PCE exceeding 22% [3, 5]. Surprisingly, the reported operational stability of some high-efficiency PSCs, where 2D structures and/or Cs have been used to improve the device stability remains low [25, 47-48]. Recently, Seo *et al.* improved the stability using poly(3-hexylthiophene) as the hole transporting material (HTM) [6]. However, the stability of their reference cell using standard Spiro-MeOTAD lagged still far behind.

We checked the phase stability of the vapor treated $FAPbI_3$ films under long term heat stress at 85 ℃ in an inert N_2 environment since $FAPbI_3$ undergoes a transition to a yellow phase below 400 K. Figure S18 shows the XRD data of the vapor treated $FAPbI_3$ films annealed up to 500 hours. It clearly shows the persistence of the black α-phase for all $FAPbI_3$ perovskite films, even after 500 hours annealing at 85 ℃, which suggests good heat stability of the vapor treated $FAPbI_3$. We also checked the shelf life of our $FAPbI_3$ based PSCs, shown in Figure S19. After 2500 hours storage in a dry box, the PCE remained at 97.8% of its initial value.

We performed long term operational stability tests for 500 hours with MPP tracking under continuous one sun illumination for our $FAPbI_3$ based PSCs. Figure 5(a) shows that the PCE of our $FAPbI_3$ based PSCs remains around 90% of the initial value (21.4%) after 500 hours MPP measurements. We also note that the PCE partially recovered to 20.2%, which is 94.4% of the initial value after 12 hours of rest in open circuit conditions in the dark. This is consistent with our previous reports [49]. The operational stability of our $FAPbI_3$ PSCs is among the top reported operational values for PSCs. As a comparison, we note that, our measured stability results are even better than that of the reported Cs and Rb co-doped $FAPbI_3$ based PSCs when

the same tin oxide based planar structure is used but without polymer passivation [4]. PV metrics derived from the J-V curves, including V_{OC}, J_{SC}, FF and the hysteresis factor (P_{for}/P_{rev}), are shown in Figures 5(b), 5(c), 5(d) and 5(e). The V_{OC} and J_{SC} remain constant during 500 hours MPP tracking and the hysteresis factor remains close to one, suggesting minimal electronic charge trapping at interfaces. We also note that the main degradation of our PSCs is due to the FF decline from 0.77 to 0.70 over the light soaking period. However, the FF largely recovers when the cell is left in the dark for a few hours as shown by the final red point in Figure 5(d). Thus, the FF is a reversible phenomenon and does not indicate permanent degradation of the device. During the long-term light soaking, the PSC is subjected to an electric field originating from the voltage difference across the device at MPP. This in turn produces migration of Li^+ ions across the film leading to a de-doping of the hole conductor. As a result, the hole transport resistance increases explaining the observed decline of FF. In the dark, the internal field vanishes, and the hole conductor will recuperate most of the Li^+ ions which leads to the recovery of FF.

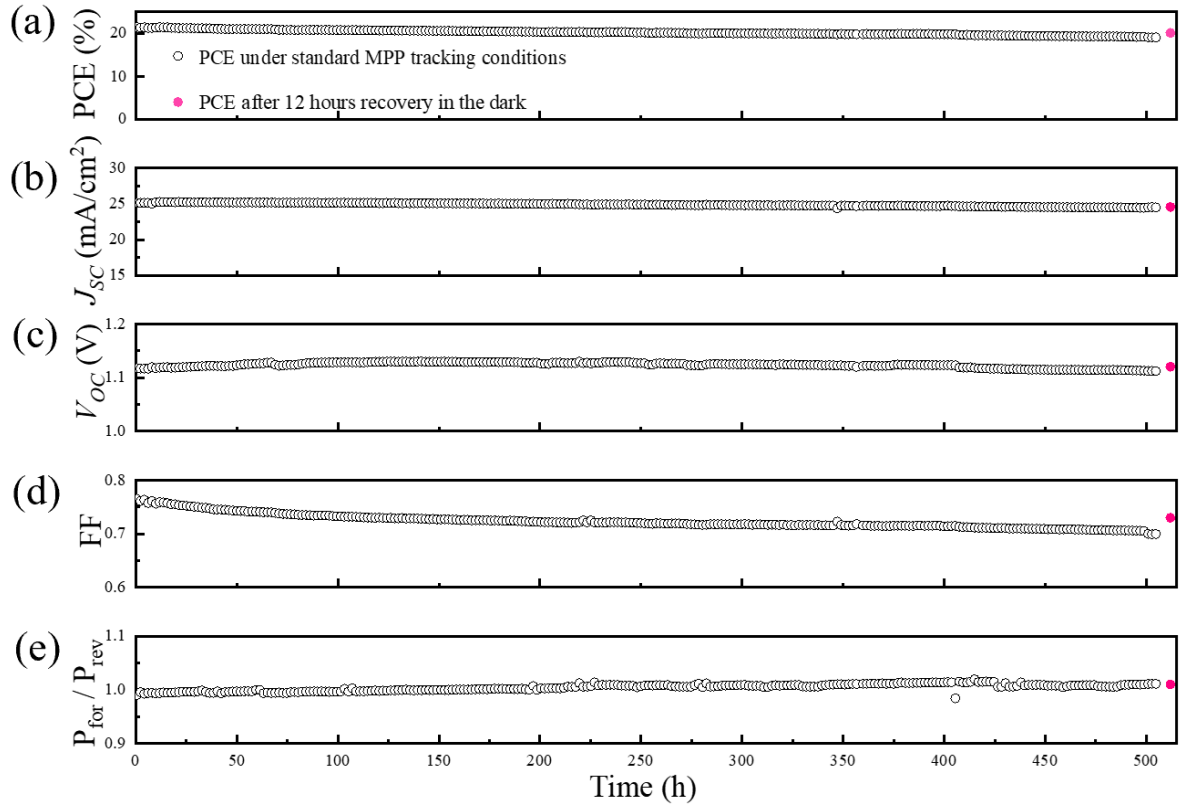

Figure 5*. Operational stability tests under 500 hours MPP tracking conditions for PCE* ***(a)****,* J_{sc} ***(b)****,* V_{oc} ***(c)****, FF* ***(d)****, and hysteresis factor (*P_{for}/P_{rev}*)* ***(e)****.*

Reference

[1] W. Nie *et al*., *Science* **347**, 522-525 (2015).
[2] M. Saliba *et al*., *Science* **354**, 206-209 (2016).
[3] W. Yang *et al*., *Science* **356**, 1376-1379 (2017).
[4] S. Turren-Cruz *et al*., *Science* **362**, 449-453(2018).
[5] Q. Jiang *et al*., *Nat. Photon.***13**, 460-466 (2019).
[6] E. Jung *et al*., *Nature* **567**, 511-515 (2019).
[7] S. Bai *et al*., *Nature* **571**, 245-250 (2019).
[8] S. Yang *et al*., *Science* **365**, 473-478 (2019).

[9] Y. Wang *et al*., *Science* **365**, 687-691 (2019).
[10] J. Tong *et al*., *Science* **364**, 475-479 (2019).
[11] K. Lin *et al*., *Nature* **562**, 245-248 (2018).
[12] Y. Cao *et al*., *Nature* **562**, 249-253 (2018).
[13] W. Xu *et al*., *Nat. Photon.* **13**, 418-424 (2019).
[14] B. Zhao *et al*., *Nat. Photon.* **12**, 783-789 (2018).
[15] T. Matsushima *et al*., *Nature* **572**, 502-506 (2019).
[16] G. Xing *et al*., *Nat. Mater.* **13**, 476-480 (2014).
[17] Y. Kim *et al*., *Nature* **550**, 87-91 (2017).
[18] W. Pan *et al*., *Nat. Photon.* **11**, 726-732 (2017).
[19] A. Kojima *et al*., *J. Am. Chem. Soc.* **131**, 6050-6051 (2009).
[20] www.nrel.gov/pv/cell-efficiency.html.
[21] D. Kubicki *et al*., *J. Am. Chem. Soc.* **139**, 10055-10061 (2017).
[22] D. Kubicki *et al*., *J. Am. Chem. Soc.* **140**, 3345-3351 (2018).
[23] Z. Wang *et al*., *Nat. Energy* **3**, 855-861 (2018).
[24] S. Draguta *et al*., *Nat. Commn*. **8**, 200 (2017).
[25] J. Lee *et al*., *Nat. Commn.* **9**, 3021 (2018).
[26] A. Swarnkar *et al*., *Science* **354**, 92-95 (2016).
[27] Y. Fu *et al*., *Nano Lett*. **17**, 4405-4414 (2017).
[28] J. Wang *et al*., *Nat. Commn*. **11**, 582 (2020).
[29] Y. Chen *et al*., *Nature* **577**, 209-215 (2020).
[30] I. Turkevych *et al*., *Nat. Nanotech*. **14**, 57-63 (2019).
[31] B. J. Foley *et al*., *J. Mater. Chem.* **5**, 113-123 (2017).
[32] M. Kim *et al*., *Joule* **3**, 1-14 (2019).
[33] H. Min *et al*., *Science* **366**, 749-753 (2019).
[34] W. Xiang *et al*., *Joule* **3**, 205-214 (2019).
[35] D. J. Kubicki *et al*., *J. Am. Chem. Soc.* **139**, 14173-14180 (2017).
[36] D. J. Kubicki *et al*., *J. Am. Chem. Soc*. **140**, 7232-7238 (2018).
[37] B. A. Rosales *et al*., *Chem. Mater.* **28**, 6848-6859 (2016).
[38] E. A. Alharbi *et al*., *Nat. Common.* **10**, 3008 (2019).
[39] M. Tavakoli *et al*., *Energy Environ. Sci.* **11**, 3310-3320 (2018).
[40] P. Ahlawat *et al*., *Chem. Mater*. **32**, 529-536 (2019).
[41] W. Tress *et al*., *Adv. Energy Mater*. **5**, 1400812 (2015).
[42] G. E. Eperon *et al*., *Energy Environ. Sci.* **7**, 982-988 (2014).
[43] M. A. Green *et al*., *Prog. Photovolt. Res. Appl.* **26**, 3-12 (2018).
[44] R. T. Ross, *J. Chem. Phys.* **46**, 4590-4593 (1967).
[45] O. D. Miller *et al*., *IEEE Journal of Photovoltaics* **2**, 303-311 (2012).
[46] J. J. Yoo *et al*., *Energy Environ. Sci.* **12**, 2192-2199 (2019).
[47] D. Yang *et al*., *Nat. Commn.* **9**, 3239 (2018).
[48] Q. Li *et al*., *Adv. Mater.* **30**, 1803095 (2018).
[49] W. Tress *et al*., *Nat. Energy*. 4, 568-574 (2019).

Acknowledgements
H.L. would like to thank the support from China Postdoctoral Science Foundation Funded Project (2017M611440). U.R. thanks the Swiss National Science Foundation through the NCCR MUST and individual grant 200020-185092. M.G. acknowledges financial support from the European Union's Horizon 2020 research and innovation programme under grant agreement No 826013 and the King Abdulaziz City for Science and Technology (KACST). A.H. acknowledges the Swiss National Science Foundation for financial support

(200021_157135/1). The authors thank F. Bobard, B. P. Darwich and W. Bi for technical support.

Author Contributions

H.L. conceived the ideas, fabricated all the devices, conducted the relevant measurements, and wrote the draft of the manuscript; P.A. and U.R. were responsible for the large-scale molecular dynamics simulations; Y.L. synthesised the necessary materials; A.M., C.A. and L.E. conducted the ssNMR measurements and analysis; B.C. helped to conduct the PL measurements; A.A. helped to conduct the long-term operational stability measurements; W.T. and F.E. conducted the EL and EQE_{EL} measurements as well as the radiative limit V_{OC} calculations; W.Z. conducted the UV-vis and XRD measurements; Y.Z., L.Z., M.G. and A.H. directed and participated in the supervision of the work. All authors analysed the data and contributed to the discussions.